Physica Medica 59 (2019) 112–116

Contents lists available at ScienceDirect

Physica Medica

journal homepage: www.elsevier.com/locate/ejmp

Original paper

Perturbation effect of parallel-plate ionization chambers on buildup dose measurements in transverse magnetic fields

Takanori Matsuoka[a], Fujio Araki[b,*], Takeshi Ohno[b]

[a] Graduate School of Health Sciences, Kumamoto University, 4-24-1 Kuhonji, Kumamoto, Japan
[b] Department of Health Sciences, Faculty of Life Sciences, Kumamoto University, 4-24-1 Kuhonji, Kumamoto, Japan

ARTICLE INFO

Keywords:
Parallel-plate ionization chamber
Transverse magnetic field
Perturbation effect
Buildup dose measurement

ABSTRACT

The aim of this study is to investigate the perturbation effect of parallel-plate ionization chambers on the buildup dose measurement in transverse magnetic fields, using Monte Carlo (MC) simulation. The NACP-02 and ROOS parallel-plate chambers and a PTW31010 cylindrical chamber were modeled for buildup dose measurement in magnetic fields, using the EGSnrc/cavity code. The irradiation condition was set to a $10 \times 10\,cm^2$ field in a water phantom at a source-to-surface distance (SSD) of 100 cm, using 6-MV photon spectrum. Magnetic fields of 0 0.35, 1.0, 1.5, and 3.0 T were applied perpendicularly to the direction of the photon beam. The overall perturbation factor $P_{Q,B}$ for the ionization chambers in the magnetic fields was also calculated. The dose to water was enhanced with increasing the magnetic field strength at a depth of less than 1 cm. Over a depth of 1.5 cm, there was no significant difference in the depth doses with and without magnetic field in water. The maximum depth dose (%) for the NACP-02 and ROOS chambers at 1.5 T was higher up to 12% and 14% than the maximum depth dose at 0 T, respectively. The depth dose curves of a PTW31010 chamber have a similar tendency to those of water. The $P_{Q,B}$ values for each chamber were the largest at the phantom surface. The transverse magnetic field has a greater effect on the dose response of the NACP and ROOS chambers than that of the PTW31010 chamber in the buildup region.

1. Introduction

Recently, magnetic resonance imaging guided radiation therapy (MRgRT), integrated with magnetic resonance (MR) device and a linear accelerator, has been developed in several countries [1,2]. This system is capable of real-time target tracking and visualizing targets by MR imaging (MRI) [3–5]. MRI is widely used as diagnostic imaging owing to its excellent visualization of soft tissues. Therefore, MRgRT can achieve spatially high dose conformity over the target while limiting the dose to normal tissues. The main challenge in the practical clinical application of MRgRT arises from secondary electrons, whose trajectories are deflected by the Lorentz force. Thus, the dose distributions in targets are disturbed by a magnetic field. The effect of the transverse magnetic field arises especially at interfaces such as lung and soft tissue or skin and air, which is known as the electron return effect (ERE) [6–8].

Specifically, the transverse magnetic field has an effect on the response of the ionization chamber [9–15]. The mean path length and the number of electrons entering the chamber air cavity vary with the Lorentz force. Therefore, the chamber response varies depending on the magnetic field strength, the magnetic field orientation with respect to the air cavity axis, and the cavity size and shape. So far, several studies have investigated the response of various detectors in transverse magnetic fields [13–17]. A significant change in the response has been observed for ionization chambers, diamond detectors, and diode detectors [14,16,17]. However, nearly all studies have been focused on the detector response at a reference depth. In addition, the depth dose in a buildup region is noticeably affected by the distortion of secondary electrons by magnetic fields [6,18]. Therefore, it is also important to investigate the detector response in the buildup region. There are only a few studies available on the dose measurement in a buildup region [16,19,20]. A higher magnetic field results in an increase in the dose in the buildup region and consequently contributes to a higher skin dose. Oborn et al. [21] have reported that 3.0 T transverse magnetic field increased a 70-μm skin dose by up to 31% for a $10 \times 10\,cm^2$ field, using a 6-MV photon beam.

The choice of the detector for the dose measurement in the buildup region is rather important because of its high dose gradient and electron disequilibrium [22,23]. Typically, parallel-plate ionization chambers have been used for dose measurements without magnetic field.

* Corresponding author.
E-mail address: f_araki@kumamoto-u.ac.jp (F. Araki).

https://doi.org/10.1016/j.ejmp.2019.03.011
Received 10 December 2018; Received in revised form 16 February 2019; Accepted 12 March 2019
Available online 14 March 2019

Table 1
Physical characteristics of the NACP-02 and ROOS parallel-plate chambers.

Chamber type	Entrance window	Body material	Electrode	Guard ring
NACP-02 0.157 cm^3	0.17 mm mylar (1.38 g/cm^3) 0.53 mm graphite (1.85 g/cm^3)	Polystyrene (1.06 g/cm^3)	Diameter: 10 mm Separation: 2.0 mm	Width: 3.0 mm
ROOS 0.382 cm^3	0.02 mm graphite (1.85 g/cm^3) 1 mm PMMA (1.19 g/cm^3)	PMMA (1.19 g/cm^3)	Diameter: 15.6 mm Separation: 2.0 mm	Width: 3.7 mm

However, it has not been thoroughly investigated if parallel-plate chambers can be used for dose measurements in magnetic field. The aim of this study is to investigate the possibility of using parallel-plate chambers for dose measurements in the buildup region in transverse magnetic field, using Monte Carlo (MC) simulation. The response of parallel-plate chambers was compared with that of a cylindrical ionization chamber with different magnetic field strengths.

2. Materials and methods

2.1. Monte Carlo depth dose calculation in a buildup region

The cavity code [24] based on the EGSnrc system [25,26] was used to model the ionization chambers. Three different chambers were used in this study, that is, NACP-02 and ROOS parallel-plate chambers and a PTW31010 cylindrical chamber. The physical characteristics of the two parallel-plate chambers and the cylindrical chamber are presented in Tables 1 and 2, respectively.

Fig. 1 illustrates the geometrical arrangement of the dose calculation in the buildup region in water. Fig. 1(a) shows the dose in a water slab, D_w, scored by a cylindrical volume of a radius of 10 mm and thickness of 0.1 mm. Fig. 1(b) and (c) show doses scored in the sensitive volume of the parallel-plate chamber and the cylindrical chamber, $D_{chamber}$. The detailed geometries and material compositions of the chambers presented in Tables 1 and 2 were modeled according to the information provided by manufacturers or previous studies [27,28]. The effective points of measurement for the parallel-plate chambers and cylindrical chamber were taken to be at front face of the chamber cavity and at 0.6r (r is radius of the chamber cavity) upstream of the cavity center, respectively.

The incident photon spectrum was obtained from a phase space file of a model for a Varian 6-MV linear accelerator. The phase space file was scored for a 10 × 10 cm^2 field at a water phantom surface at a source to surface distance (SSD) of 100 cm. Since the electrons generated in the linac head or air column are removed by transverse magnetic fields, the photon spectrum was used in this study [20,21]. The static transverse magnetic flux densities of 0, 0.35, 1.0, 1.5, and 3.0 T were oriented perpendicularly to the incident photon beam. The magnetic field and long axis of the cylindrical chamber cavity were parallel with each other. The relative depth dose, RDD (%), of the water slab and relative depth response, RDR (%) of the ionization chambers in the buildup region in the magnetic field, B, was adjusted to correspond to the measured percentage depth dose, PDD (10, 10 × 10), at a depth of 10 cm for a 10 × 10 cm^2 field without magnetic field as follows:

$$\mathrm{RDD}(d,\quad 10\times 10)_B = \frac{[D_w(d,\ 10\times 10)]_B}{[D_w(10,\ 10\times 10)]_{B=0}} \times \mathrm{PDD}(10,\quad 10\times 10)_{B=0}, \tag{1}$$

$$\mathrm{RDR}(d,\quad 10\times 10)_B = \frac{[D_{\mathrm{chamber}}(d,\ 10\times 10)]_B}{[D_{\mathrm{chamber}}(10,\ 10\times 10)]_{B=0}} \times \mathrm{PDD}(10,\quad 10\times 10)_{B=0}. \tag{2}$$

In the simulations, the photoelectron angular sampling, atomic relaxation, spin-effect, and electron impact ionization were included. The XCOM database [29] from the National Institute of Standards Technology (NIST) was used for the photon cross section. The EXACT algorithm and PRESTA-II algorithm were used for the boundary crossing algorithm and electron-step algorithm, respectively. The emf macros, developed for the EGS4 by Bielajew [30], was used to calculate the electron transport in the presence of the magnetic field. Recently, the new emf macros algorithm has been implemented to improve on the previous EGS4 magnetic field macros package introduces a specialized single scatter algorithm, and allows for proper boundary crossing [31]. The EGSnrc code is validated by a new Fano test that accommodates an external magnetic field. In this study the new emf macros was used and the value of EM ESTEPE was set to 0.02, which is the step size restrictions based on energy loss, change in the magnetic field strength and direction. The value of EM ESTEPE has been validated by the Fano cavity test in previous studies [13,18,31,32]. For the efficient calculation, the photon splitting and variance reduction techniques were used. The photon and electron cutoff energies used in the simulation were 10 keV and 521 keV, respectively. The statistical uncertainty of the calculated dose in the chamber cavity was less than 0.2% in one standard deviation.

2.2. Perturbation correction factor for chambers in magnetic fields

The overall perturbation correction factor, P_Q, for the parallel-plate and cylindrical ionization chambers can be expressed according to the Spencer–Attix cavity theory as

$$P_Q = [(D_w/\bar{D}_{\mathrm{chamber}})/(\bar{L}/\rho)^w_{\mathrm{air}}]_{B=0}, \tag{3}$$

where $(\bar{L}/\rho)^w_{\mathrm{air}}$ is the average restricted water-to-air collision stopping power ratio, which was calculated by the EGSnrc/SPRRZ code [33]. In transverse magnetic fields, the secondary electrons are deflected in the air cavity. The perturbation correction factor $P_{Q,B}$ in applied magnetic field, B, is given by

$$P_{Q,B} = [(D_w/\bar{D}_{\mathrm{chamber}})/(\bar{L}/\rho)^w_{\mathrm{air}}]_B. \tag{4}$$

where, $(\bar{L}/\rho)^w_{\mathrm{air}}$ is calculated in the magnetic field.

Table 2
Physical characteristics of the PTW31010 (0.125 cm^3) cylindrical chamber.

Chamber type	Wall of sensitive volume	Dimension of sensitive volume	Central electrode
PTW31010 0.125 cm^3	0.55 mm PMMA (1.19 g/cm^2) 0.15 mm graphite (0.82 g/cm^2)	Radius: 2.75 mm Length: 6.5 mm	Aluminum Diameter: 1.1 mm

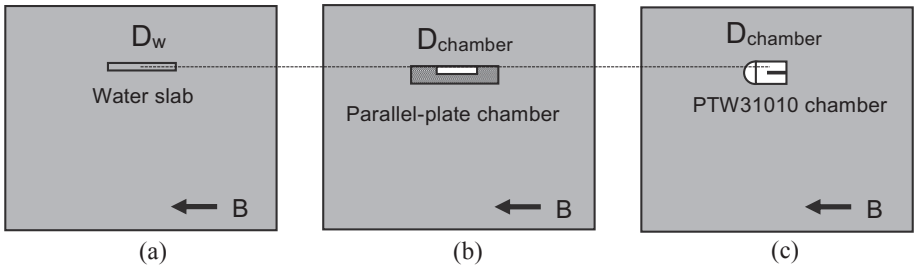

Fig. 1. Simplified geometrical arrangement of dose calculations in the buildup region for different detectors: (a) water slab (b) NACP-02 and ROOS chambers, and (c) PTW31010 chamber. The effective points of measurement are taken to be at the front face of the cavity for the parallel-plate chambers and at 0.6*r* (*r* is radius of the chamber cavity) upstream of the cavity center for the cylindrical chamber.

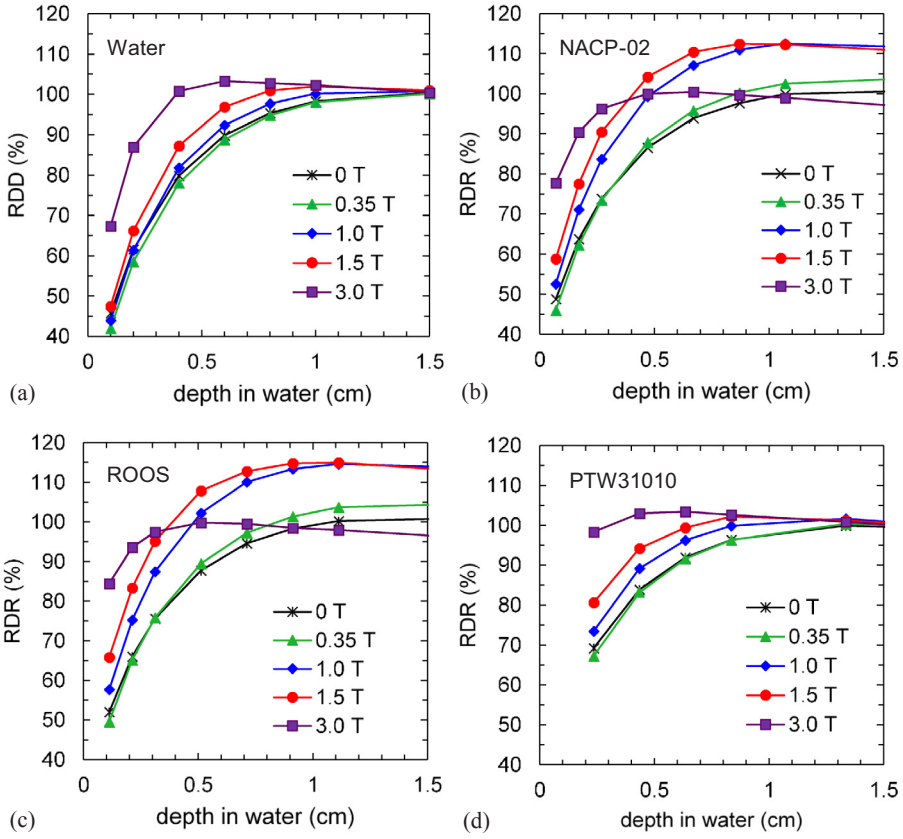

Fig. 2. Comparison of relative depth doses (RDD) and relative depth responses (RDR) in a buildup region at a 10 × 10 cm^2 field in magnetic fields of 0, 0.35, 1.0, 1.5, and 3.0 T: (a) water slab, (b) NACP-02, (c) ROOS, and (d) PTW31010 chambers. The dose in different chambers is adjusted to correspond to the measured percentage depth dose at a depth of 10 cm without magnetic field.

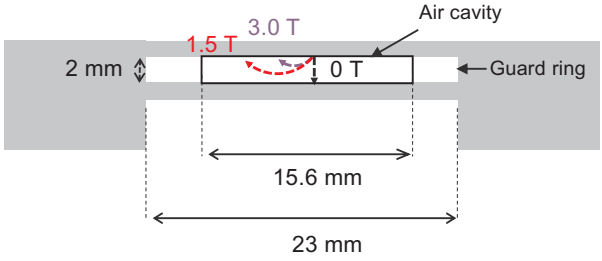

Fig. 3. Electron trajectories in the air cavity of the ROOS chamber at a depth of 1.0 cm with a mean radius of 0.34 cm and 0.17 cm for transverse magnetic fields of 1.5 T and 3.0 T, respectively. The trajectories are indicated by dotted lines.

3. Results and discussion

3.1. Depth dose in the buildup region

Fig. 2(a)–(d) show the calculated depth dose curves of the water slab, NACP-02, ROOS, and PTW31010 chambers in the buildup region in water, respectively. The depth of the dose maximum (d_{max}) shifted toward the surface as the transverse magnetic field was increased. The trajectories of the secondary electrons are deflected by the Lorentz force and consequently, depending on the magnetic field strength, they result in a shorter longitudinal electron range and eventually resulting in a shallower buildup range [12].

As can be seen in Fig. 2(a), the dose to water enhanced with the increase of the magnetic field strength at a depths less than 1 cm. Specifically, the maximum depth dose at 0.6 cm in 3.0 T was higher up to 3% than that at 1.5 cm in 0 T and the depth dose at 0.1 cm was higher up to 47% than that of 0 T. The difference in the depth dose with and without the magnetic field was constant within 1% at a transient electron equilibrium region over the depth of 1.5 cm [13].

The response of a NACP-02 chamber, shown in Fig. 2(b), has a slightly complicated dose buildup. The maximum depth dose at around 1 cm in 1.5 T was higher up to 12% than that at 1.5 cm in 0 T, whereas it decreased over the depth of around 0.7 cm at 3.0 T. A similar tendency was observed for a ROOS chamber as well, as shown in Fig. 2(b). The maximum depth dose in 1.5 T was higher up to 14%. This is a typical phenomenon for two parallel-plate chambers. The secondary electrons in the chamber air cavity are deflected by the transverse magnetic field. It is considered that the dose in the chamber cavity is enhanced with the increase of the mean path electron length in the

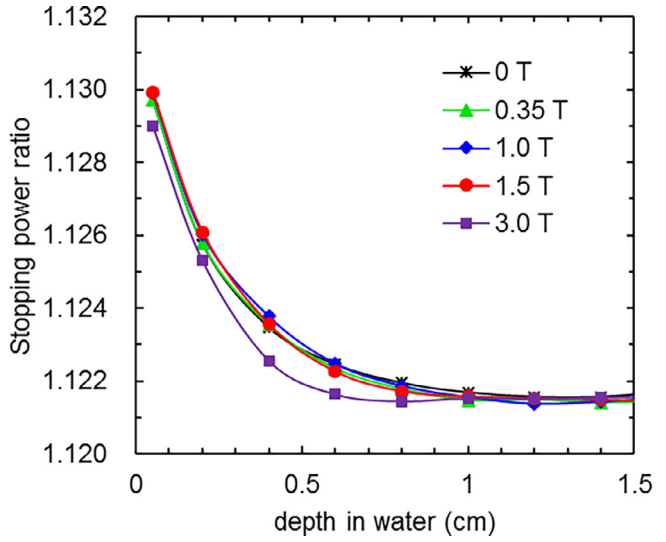

Fig. 4. Comparisons of average restricted collision stopping power ratios of water to air in transverse magnetic fields. The stopping power rations were calculated by the EGSnrc/SPRRZnrc code.

cavity, which is associated with the gyro radius and range of secondary electrons. The gyro radius r of secondary electrons can be expressed as

$$r = \frac{mv}{eB}, \tag{5}$$

where m is the electron mass (kg), v is the electron velocity (m/s), e is the elementary charge (C), and B is the magnetic flux density (T).

Fig. 3 shows the electron trajectories in the air cavity for the ROOS chamber. The mean electron energy at a depth of 1.0 cm for a 6-MV photon beam was 1.09 MeV, obtained from the electron fluence spectrum calculated by the EGSnrc/flurznrc code [33]. Thus, according to Eq. (5), the gyro radius was 0.51 cm for 1.0 T, 0.34 cm for 1.5 T and 0.17 cm for 3.0 T. The mean path length of the distorted secondary electrons in the air cavity was longer in the transverse magnetic field of 1.0 and 1.5 T than that in the air cavity without magnetic field. Consequently, the dose in the air cavity rapidly increases at 1.0 and 1.5 T. In contrast, the dose in the air cavity in 3.0 T decreases at the region beyond the transient electron equilibrium at a depth of approximately 0.5 cm. This is because the mean electron path length in the air cavity in 3.0 T is shorter than that in 1.0 and 1.5 T. It should be noted that most of the incoming secondary electrons enter the magnetic field in the air cavity under an oblique angle of approximately 40° [34]. At a transient electron equilibrium region, the difference in the depth dose with and without the magnetic field increased by 9.0% for NACP-02 and 10.6% for ROOS at 1.0 T and it was constant. The dose difference also corresponds to reciprocal of the overall perturbation correction factor presented in Eq. (4).

The effect of the inflected secondary electrons on the dose varies depending on the sensitive volume in the air cavity; for example, the NACP-02 and ROOS chamber has a larger effect on the dose than that of a PTW31010 chamber. The depth dose curves of a PTW31010 chamber, shown in Fig. 2(d), have a similar tendency to those of water. This is because the shape of the air cavity is cylindrical and the Lorentz force is parallel with the short axis in the air cavity. There was no significant difference more than 1.0% in the RDR (%) with and without the magnetic field at a transient electron equilibrium region.

Fig. 4 presents the averaged restricted collision stopping power ratios of water to air in transverse magnetic fields. The difference in the stopping power ratios between 0 T and 3.0 T was less than 0.2%. The values were used to determine the perturbation correction factor $P_{Q,B}$ in Eqs. (3) and (4).

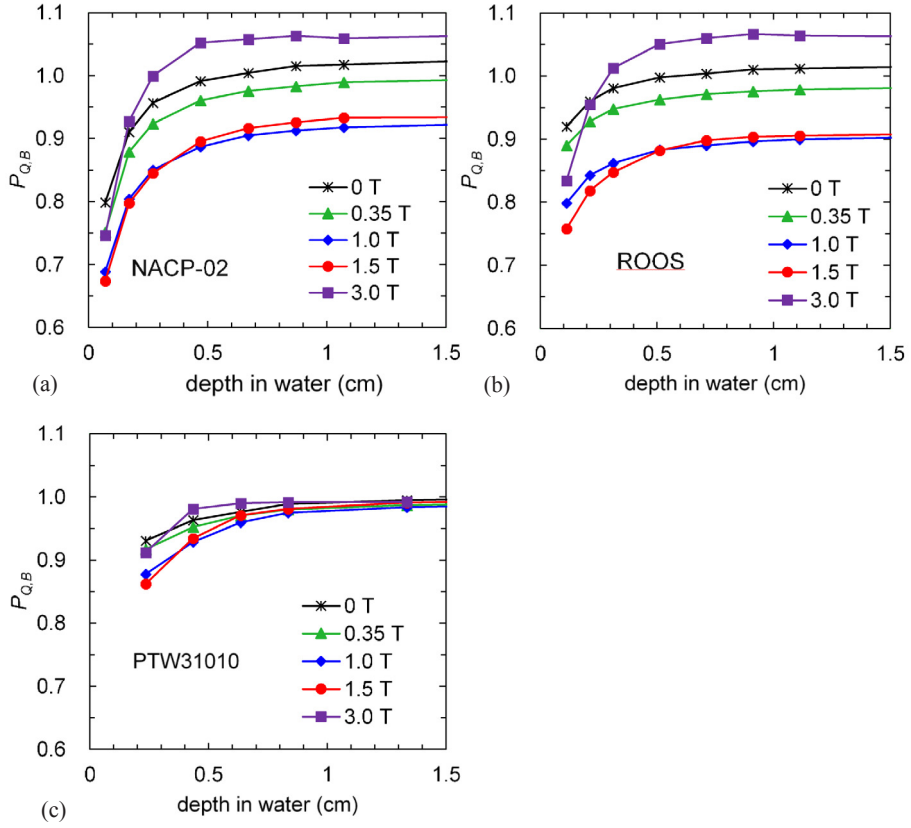

Fig. 5. Comparison of perturbation correction factors $P_{Q,B}$ in a buildup region at a 10 × 10 cm^2 field in the magnetic fields of 0, 0.35, 1.0, 1.5, and 3.0 T: (a) NACP-02, (b) ROOS, and (c) PTW31010 chambers.

The perturbation correction factor $P_{Q,B}$ for the NACP-02, ROOS, and PTW31010 chambers in the transverse magnetic field are shown in Fig. 5(a)–(c). The perturbation effect for each chamber was the largest at the phantom surface, and the $P_{Q,B}$ values for the NACP-02, ROOS, and PTW31010 chambers were 0.674, 0.758, and 0.862 in a magnetic field of 1.5 T, respectively. The $P_{Q,B}$ values for the NACP-02 and ROOS chambers strongly vary depending on the magnetic field strength. This is because the electron trajectories inflected in the air cavity of the parallel-plate chamber are significantly longer than those of the PTW31010 chamber, as shown in Fig. 3. The $P_{Q,B}$ values are also constant when a transient electron equilibrium is achieved and correspond to those at a reference depth of 10 cm. In addition, the $P_{Q,B}$ values for the NACP-02, ROOS, and PTW31010 chambers at a reference depth of 10 cm were 0.920, 0.903, and 0.994 at a magnetic field of 1.5 T, respectively, and they were in a good agreement within 1% with those by Malkov et al. [15]. The $P_{Q,B}$ values for the PTW31010 chamber were close to unity with a small variation depending on the magnetic field strength. This is because the mean electron path length is nearly the same with and without the magnetic field at the short axis due to the rotational symmetry of the air cavity.

4. Conclusions

The transverse magnetic field has a greater effect on the dose measurement response of NACP and ROOS parallel-plate chambers than that of a PTW31010 cylindrical chamber in the buildup region. The overall perturbation correction factor for parallel-plate ionization chambers were significantly larger than that of the cylindrical chamber in the magnetic field. Therefore, cylindrical chambers with small air cavity may be suitable for buildup dose measurements in transverse magnetic fields. In addition, the perturbation factors must be calculated for each chamber in order to make the accurate dose measurements in the buildup region.

References

[1] Raaymakers BW, Lagendijk JJW, Overweg J, Kok JG, Raaijmakers AJ, Kerkhof EM, et al. Integrating a 1.5 T MRI scanner with a 6 MV accelerator: proof of concept. Phys Med Biol 2009;54:229–37.

[2] Lagendijk JJW, Raaymakers BW, van Vulpen M. The magnetic resonance imaging-linac system. Semin Radiat Oncol 2014;24:207–9.

[3] Lagendijk JJW, Raaymakers BW, Raaijmakers AJ, Overweg J, Brown KJ, Kerhof EM, et al. MRI/linac integration. Radiother Oncol 2008;86:25–9.

[4] Raaijmakers AJE, Raaymakres BW, Lagendijk JJW. Magnetic field induced dose effects in MR-guided radiotherapy systems: dependence on the magnetic field strength. Phys Med Biol 2008;53:909–23.

[5] Kolling S, Oborn B, Keall P. Impact of the MLC on the MLC field distortion of a prototype MRI-linac. Med Phys 2013;40:121705.

[6] Raaymakers BW, Raaijmakers AJE, Kotte ANTJ, Jette D, Lagendijk JJ. Integrating a MRI scanner with a 6 MV radiotherapy accelerator: dose deposition in a transverse magnetic field. Phys Med Biol 2004;49:4109–18.

[7] Raaijmakers AJE, Raaymakers BW, Lagendijk JJW. Integrating a MRI scanner with a 6 MV radiotherapy accelerator: dose increase at tissue-air interfaces in a lateral magnetic field due to returning electrons. Phys Med Biol 2005;50:1363–76.

[8] Raaijmakers AJ, Raaymakers BW, van der Meer S, Lagendijk JJ. Integrating a MRI scanner with a 6 MV radiotherapy accelerator: impact of the surface orientation on the entrance and exit dose due to the transverse magnetic field. Phys Med Biol 2007;52:929–39.

[9] Meijsing I, Raaymakers BW, Raaijmakers AJ, Kok JG, Hogeweg L, Liu B, et al. Dosimetry for the MRI accelerator: the impact of a magnetic field on the response of a Farmer NE 2571 ionization chamber. Phys Med Biol 2009;54:2993–3002.

[10] Reynolds M, Fallone BG, Rathee S. Dose response of selected ion chambers in applied homogeneous transverse and longitudinal magnetic fields. Med Phys 2013;40. 042102-1-7.

[11] O'Brien DJ, Robarts DA, Ibbott GS, Sawakuchi GO. Reference dosimetry in magnetic fields: formalism and ionization chamber correction factors. Med Phys 2016;43:4915–27.

[12] Agnew J, O'Grady F, Young R, Duane S, Budgell GJ. Quantification of static magnetic field effects on radiotherapy ionization chambers. Phys Med Biol 2017;62:1731–43.

[13] Spindeldreier CK, Schrenk O, Bakenecker A, Kawrakow I, Burigo L, Karger CP, et al. Radiation dosimetry in magnetic fields with Farmer type ionization chambers: determination of magnetic field correction factors for different magnetic field strength and field orientations. Phys Med Biol 2017;62:6708–28.

[14] Malkov VN, Rogers DWO. Monte Carlo study of ionization chamber magnetic field correction factors as a function of angle and beam quality. Med Phys 2018;45:908–25.

[15] Pojtinger S, Dohm OS, Kapsch RP, Daniela Thorwarth D. Ionization chamber correction factors for MR-linacs. Phys Med Biol 2018;63:8.

[16] Reynolds M, Fallone BG, Rathee S. Dose response of selected solid state detectors in applied homogeneous transverse and longitudinal magnetic fields. Med Phys 2014;41:092103.

[17] Malkov VN, Rogers DWO. Sensitive volume effects on Monte Carlo calculated ion chamber response in magnetic fields. Med Phys 2017;44:4854–8.

[18] Ghila A, Steciw S, Fallone BG, Rathee S. Experimental verification of EGSnrc Monte Carlo calculated depth doses within a realistic parallel magnetic field in a polystyrene phantom. Med Phys 2017;44:4804–12.

[19] Oborn BM, Metcalfe PE, Butson MJ, Rosenfeld AB. Monte Carlo characterization of skin doses in 6 MV transverse field MRI linac systems: effect of field size, surface orientation, magnetic field strength, and exit bolus. Med Phys 2010;37:5208–17.

[20] Wegener S, Weick S, Sauer OA. Influence of a transverse magnetic field on the response of different detectors in a high energy photon beam near the surface. Z Med Phys 2019;29:22–30.

[21] Oborn BM, Metcalfe PE, Butson MJ, Rosenfeld AB. High resolution entry and exit Monte Carlo dose calculations from a linear accelerator 6 MV beam under the influence of transverse magnetic fields. Med Phys 2009;36:3549–59.

[22] Gerbi BJ, Khan FM. Measurement of dose in the buildup region using fixed-separation plane-parallel ionization chambers. Med Phys 1990;17:17–26.

[23] Rawlinson J, Arlen D, Newcombe D. Design of parallel plate ion chambers for buildup measurements in megavoltage photon beams. Med Phys 1992;19:641–8.

[24] Kawrakow I, Mainegra-Hing E, Tessier F, et al. EGSnrc C++ class library, National Research Council Canada Report PIRS-898. 2018.

[25] Kawrakow I. Accurate condensed history Monte Carlo simulation of electron transport. I. EGSnrc, the new EGS4 version. Med Phys 2000;27:485–98.

[26] Kawrakow I, Rogers DW. The EGSnrc code system: Monte Carlo simulation of electron and photon transport. National Research Council of Canada Report PIRS-701. 2001.

[27] Chin E, Shipley D, Bailey M, Seuntjens J, Palmans H, Dusautoy A, et al. Validation of a Monte Carlo model of a NACP-02 plane-parallel ionization chamber model using electron backscatter experiments. Phys Med Biol 2008;53:119–26.

[28] Zink K, Wulff J. Monte Carlo calculations of beam quality correction factors k_Q for electron dosimetry with a parallel-plate Roos chamber. Phys Med Biol 2008;53:1595–607.

[29] Berger MJ, Hubbell JH. XCOM: Photon Cross Sections on a Personal Computer Report NBSIR87-3597 MD 20899 Gaithersburg: National Institute of Standards Technology; 1987/1999.

[30] Bielajew AF. The effect of strong longitudinal magnetic fields on dose deposition from electron and photon beams. Med Phys 1993;20:1171–9.

[31] Malkov VN, Rogers DWO. Charged particle transport in magnetic fields in EGSnrc. Med Phys 2016;44:4447–58.

[32] Lee J, Lee J, Ryu D, Lee H, Ye SJ. Fano cavity test for electron Monte Carlo transport algorithms in magnetic fields: comparison between EGSnrc, PENELOPE, MCNP6 and Geant4. Phys Med Biol 2018;63:11.

[33] Rogers DW, Kawrakow I, Seuntjens JP, Walters BRB, Mainegra-Hing E. NRC user codes for EGSnrc. National Research Council of Canada Report PIRS-702 (rev C). 2017.

[34] O'Brien DJ, Sawakuchi GO. Monte Carlo study of the chamber-phantom air gap effect in a magnetic field. Med Phys 2017;44:3830–8.